Progress In Electromagnetics Research C, Vol. 118, 187–198, 2022

Design of Hemispherical Patch Antenna with Conformally Spaced Log-Periodic Elements for Multi-Directional and Multi-Band Operation

Venkatesh Nuthan Prasad[1, *], Eshwar Dhanush Gowda[2], Krishnappa Indira[1], Ananya Kodukula[3], and Diksha Arora[4]

Abstract—In this paper, the design of an Ultra Wide Band (UWB) hemispherical antenna with Log-Periodic Elements (LPEs) capable of operating at multiple resonating frequencies lying in L, S, C, X, and Ku frequency bands is presented. The design consists of a complex structure of silver hemisphere with LPE mounted on an FR-4 substrate fed by a 50 Ω microstrip line. The dependency of the inclination of log-periodic elements mounted on the hemisphere is analyzed with parametric study. The proposed miniaturized antenna uses LPEs to obtain an impedance bandwidth of above 100% and a multi-directional radiation pattern. The measured results show that a wide operating band of 12.63 GHz (1.68 GHz–14.31 GHz) (8.52 : 1) has been achieved with a multi-directional radiation pattern with a peak realized gain of 8.12 dBi.

1. INTRODUCTION

Antenna is a key element in wireless telecommunication systems. Different types of antennas for various applications have been developed and investigated. The current trend and demands from end users are light weight and compact devices with enhanced performance. As the dimensions are small, they occupy very little space in systems. Over the past few years, the demand for antennas which are miniaturized and can offer competent performance for numerous implementations has significantly risen. The applications like GSM, WiMAX, IMT-2000, Wireless Area Networks, and computer networks use L, S, C, and X bands. Cloud computing devices, direct broadcast satellite services, and Multi-Protocol Label Switching (MPLS) use Kurz-under (Ku) bands. Airport Surface Detection Equipment (ASDE) uses Kurz (K) band radars as they provide high resolution and are suitable for short range communication.

The design of a multi-band patch antenna is significant today as it would enable the utilization of a single antenna for multiple wireless applications. Hemispherical antennas have interestingly become quite an active topic of research. Several studies have been conducted on spherical structures consisting of an array of antennas [1–12].

Multi-polarization and multi-directional energy harvesting antenna array would be conformed to a hemispherical ground plane. The hemispherical antenna provides better reception of incoming signals in all the directions by the virtue of its physical design [13].

The degree of inappropriateness in the spatial aliasing, antenna positioning, and measurement noise are assessed by the analysis of spherical antenna array via spherical harmonics decomposition

Received 4 October 2021, Accepted 12 February 2022, Scheduled 23 February 2022
* Corresponding author: Venkatesh Nuthan Prasad (nuthan.v@msrit.edu).
[1] Department of Electronics and Communication Engineering, Ramaiah Institute of Technology, Bangalore, India. [2] Robot Bosch, India. [3] Department of Computer Science and Engineering, Ramaiah Institute of Technology, India. [4] Department of Mechanical Engineering, Ramaiah Institute of Technology, India.

using Gaussian, equiangular, and uniform spatial sampling techniques for the antenna array elements positioning on a sphere [14].

Patch antennas have been gaining importance in electromagnetic devices owing to useful features such as simplicity of fabrication, low cost, minimal weight, and negligible body effect [14, 15]. However, one area that these antennas lack is bandwidth enhancement for practical applications. There exist a multitude of ways to solve this concern. The patch antenna bandwidth is inversely proportional to the quality factor. The quality factor in turn depends on substrate parameters such as dielectric constant, ε_r and substrate thickness, via inverse and direct relation, respectively [16]. The effect of increasing the thickness of the substrate and lowering dielectric constant, ε_r leads to an increase in surface wave power levels which result in poor radiation efficiency [14].

The design of UWB antennas facilitates high data rate applications for real time video and data transmission and would be most desirable in military and aerospace applications.

Summarizing the constituents of this paper, Section 2 examines the design procedure of the envisioned antenna, including its operation and geometry. Section 3 highlights the simulation results and the assessment of the proposed antenna design. Section 4 details the validation of proposed antenna design, and lastly the result is covered in Section 5.

2. ANTENNA DESIGN PROCEDURE

The model of proposed antenna is initialized by determining the number of log-periodic cylindrical silver elements having uniform radius of 0.3 mm and varying length as a function of scaling factor τ [17, 21] given in Eq. (1), where L_n is the length of the nth log-periodic element ($1 \leq n \leq 10$). The total surface area (A) of the hemisphere is calculated using Eq. (2).

$$\frac{1}{\tau} = \frac{L_n}{L_{n+1}} \tag{1}$$

$$A = 3\pi R_h^2 \tag{2}$$

LPEs are mounted onto the solid silver hemisphere of radius $R_h = 3.978$ mm having total surface area of 14.914 mm^2. The effective radius of base of the hemisphere is calculated using Eq. (3) plugging in the geometrical parameters of the prototyping antenna (R_h and T_s).

$$R_{he} = R_h \left[1 + \frac{2T_s}{\pi\varepsilon_r R_h}\left(\ln\left(\frac{\pi R_h}{2T_s}\right) + 1.7726\right)\right]^{\frac{1}{2}} \tag{3}$$

The antenna is excited with TM_{11}^{z} mode [13, 14]. The zeros X_{ij} of the derivative Bessel function $J_m(x)$ determine the order of resonating frequencies. The first value of X_{ij} is $X_{11} = 1.8412$, and the resonant frequency fr_{11} is calculated as 10.38 GHz using Eq. (4).

$$fr_{ij} = \frac{x_{ij}C}{2\pi R_{he}\sqrt{\varepsilon_r}} \tag{4}$$

where C is the speed of light in vacuum. Fig. 1(a) and Fig. 1(b) show the designed antenna with 50 Ω feed impedance and side view of the hemisphere along with cylindrical silver elements mounted on it, respectively.

The length of the longest (major) ($L_{\max} = L_1$) and shortest ($L_{\min} = L_{11}$) elements is calculated using Eq. (5).

$$L_{(\max,\min)} = \frac{\lambda_{(\max,\min)}}{2\sqrt{\varepsilon_e}} \tag{5}$$

The effective permittivity $\varepsilon_e = 3.33$ [16] is calculated using Eq. (6) as

$$\varepsilon_e = \frac{\varepsilon_r + 1}{2} + \frac{\varepsilon_r - 1}{2} \times \frac{1}{\sqrt{1 + \dfrac{12 \times T_s}{W_{f50}}}} \tag{6}$$

The width-to-height $\left(\frac{W_{f50}}{T_s}\right)$ ratio of microstrip line is 1.861, and characteristic impedance of 50 Ω and $\frac{\lambda}{4}$ microstrip line is calculated using Eq. (7) as

$$Z_0 = \frac{60}{\sqrt{\varepsilon_e}\ln\left(\frac{8T_s}{W} + \frac{W}{4T_s}\right)} \tag{7}$$

where W is the width of 50 Ω feed line or quarter wave transformer $\left(\frac{\lambda}{4}\right)$. The antenna under consideration in this paper has dimensions as shown in Table 1.

Table 1. Design parameters.

Parameters	Description	Value	Unit
$f_{\min}$	Minimum frequency	3.12	GHz
$f_{\max}$	Maximum frequency	13.32	GHz
R_h	Hemisphere radius	3.978	mm
T_s	Thickness of substrate	1.0	mm
T_p	Thickness of patch	0.035	mm
W_s	Width of substrate	25.0	mm
L_s	Length of substrate	37.018	mm
T_g	Thickness of ground	0.035	mm
W_g	Width of ground	25.0	mm
L_g	Length of ground	37.018	mm
N	Number of elements	11	-
W_{f50}	Width of 50 Ω feed	1.861	mm
L_{f50}	Length of 50 Ω feed	10.0	mm
$L_{\frac{\lambda}{4}}$	Length of $\frac{\lambda}{4}$ strip	17.048	mm
$W_{\frac{\lambda}{4}}$	Width of $\frac{\lambda}{4}$ strip	1.062	mm
L_1	Length of longest element	26.315	mm
L_{11}	Length of shortest element	6.171	mm

The hemisphere is placed on an FR-4 substrate (thickness, $T_s = 1.0$ mm and relative dielectric constant, $\varepsilon_r = 4.4$). A finite copper trace at bottom of the substrate acts as ground plane having dimensions 37.018 mm × 25.0 mm. The radiation efficiency deterioration is generally associated with the use of substrate having high dielectric constant [18]. The elements are placed with decreasing lengths from pole to base region of the hemisphere and are conformally spaced with their positions defined by angles rather than distances.

The inclination angles $\phi 1$ and $\phi 2$ are considered for elements measured along θ and ϕ in the spherical coordinate system respectively as shown in Fig. 1(c). The elements are represented by circle (major element) and ellipses (minor elements) on the surface of the hemisphere as shown in Fig. 1(d).

The angles of inclination (AoI) $\phi 1$ and $\phi 2$ are varied in the range [12°, 39°] and [15°, 25°] in steps of 10 respectively within the specified limit, and parametric simulations are carried out, yielding 308 combinations. At extreme angles as shown in Fig. 2, elements overlap with other elements and generate erroneous results. The angles are chosen such that elements do not overlap with substrate and other elements as shown in Fig. 3, which may lead to erroneous results during computation.

In order to study the effect of LPE position and inclination, each element is allowed to take two degrees of freedom with respect to AoI with reference to the origin. The AoI also governs the position of elements along the hemisphere, such that the longest element is fixed at the origin of the hemisphere. The inter-elemental distance is not linear and changes accordingly with AoI along the surface of the hemisphere as shown in Fig. 4. The arc distance C_n between any two elements specified by the angles

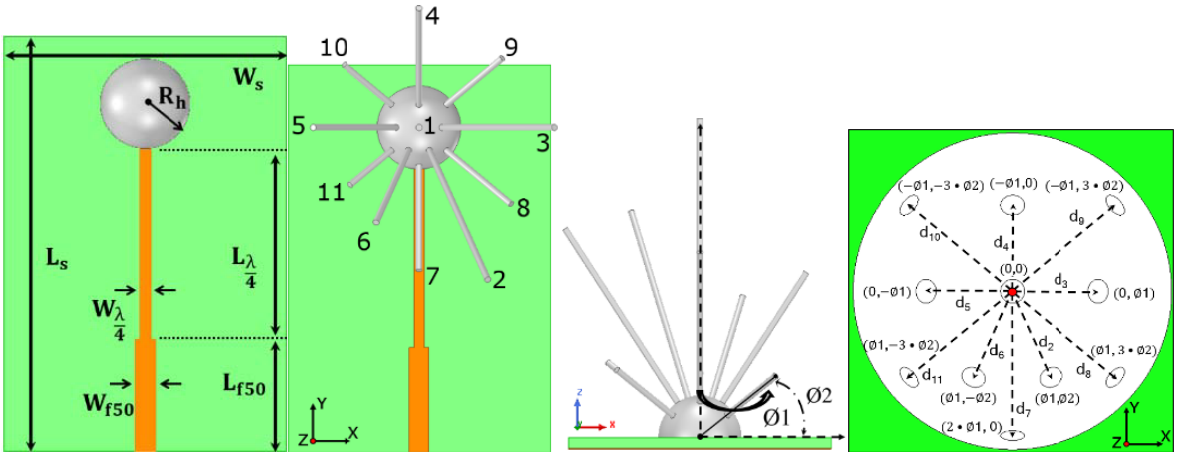

(a) (b) (c) (d)

Figure 1. The physical structure of the proposed antenna used in the simulation. (a) Antenna without elements (Ant_1). (b) Antenna with elements (Ant_2) ($\phi1 = 33°$ and $\phi2 = 17°$). (c) Side view along with inclination angles. (d) 2D top view of hemisphere illustrating position of minor elements from central major element.

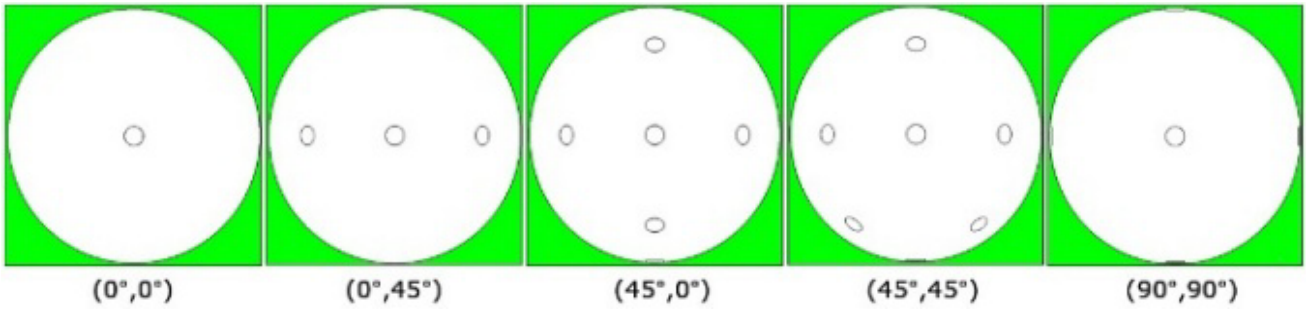

Figure 2. Elements positioned at extreme angles $(\phi1, \phi2)$ overlapping with other elements.

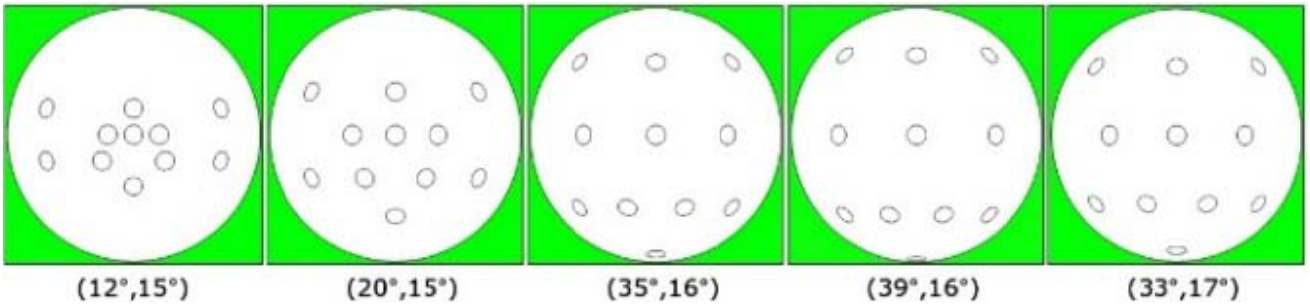

Figure 3. Position of elements on the hemisphere at chosen combinations of $(\phi1, \phi2)$ without overlapping on other elements.

$(\phi1', \phi2')$ and $(\phi1, \phi2)$ in a 3D space is computed with the aid of Cartesian subtraction [19] using Eqs. (8) and (9).

$$d_n = \sqrt{(\Delta X)^2 + (\Delta Y)^2 + (\Delta Z)^2} \tag{8}$$

where

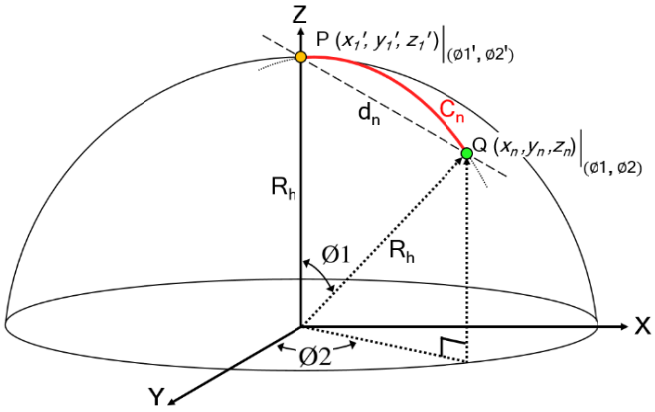

Figure 4. Arc length calculation between P and Q points on hemisphere.

$$\Delta X = (x_1' - x_n) = R_h\left(\cos\phi 1' \cos\phi 2' - \cos\phi 1 \cos\phi 2\right)$$
$$\Delta Y = (y_1' - y_n) = R_h\left(\cos\phi 1' \sin\phi 2' - \cos\phi 1 \sin\phi 2\right)$$
$$\Delta Z = (z_1' - z_n) = R_h\left(\sin\phi 1' - \sin\phi 1\right)$$

$$C_n = 2R_h \sin^{-1}\left(\frac{d_n}{2R_h}\right) \tag{9}$$

where (x_1', y_1', z_1') for $(\phi 1', \phi 2') = (0°, 0°)$ and $(x_n, y_n, z_n)\forall(\phi 1, \phi 2)(\phi 1', \phi 2') = (0°, 0°)$ are the coordinates of major elements and minor elements, respectively. Each element of antenna picks up a different frequency corresponding to its length being approximately equal to $\left(\frac{\lambda}{2}\right)$ and resonates in the active region whereas other elements behave as reactive components. All the elements are designed with a uniform radius of $R_e = 0.3\,\text{mm}$. The longest element is placed at the pole of the hemisphere, and the minor elements are placed circularly in increasing order of lengths from the left portion of the feed with increments in height over the hemisphere. The elements, which are placed in close proximity to the input feed, cancel each other's radiation out owing to being nearly out of phase. The active region varies between the elements whose length is approximately equal to half the wavelength of corresponding frequency [20].

To match the impedance between the source and load, a quarter wave impedance transformer [16] is designed between source feed line and the load. The impedance of $\left(\frac{\lambda}{4}\right)$ transformer strip is the geometric mean of source characteristic impedance Z_0 and load resistance R_L and is calculated using Eq. (10) as

$$Z_{\frac{\lambda}{4}} = \sqrt{Z_0 R_L} \tag{10}$$

where R_L is the load resistance.

The length of the quarter wave transformer is calculated using Eq. (11) as

$$L_{\frac{\lambda}{4}} = \frac{\lambda}{4\sqrt{\varepsilon_e}} \tag{11}$$

The characteristic impedance of the cylindrical elements [11] are calculated using Eq. (12) as

$$Z_e = 120 \times \left[\ln\left(\frac{L_e}{R_e}\right) - 2.25\right] \tag{12}$$

where L_e is the length of element.

Width-to-height ratio of $\left(\frac{\lambda}{4}\right)$ strip is maintained to match the impedance calculated in Eq. (7), and also the length is designed to obtain 90° phase shift. The quarter wave transformer strip line matches input feed impedance with the load resistance, ensuring minimum reflection from the load to source. As a result, standing waves are generated in $\left(\frac{\lambda}{4}\right)$ strip. Multiple reflections occur between the source and load due to the presence of different impedance strips. The input power may not be able to radiate

completely from the antenna due to the presence of impedance mismatch at various junctions. The mismatch loss ψ is a function of reflection coefficient and is computed based on Eq. (13) as

$$\psi = -10\log\left(1-\gamma^2\right) \tag{13}$$

The antenna scaling factor is chosen to be $\tau = 0.865$, and each element is designated with a diameter of $D_e = 0.3\,\text{mm}$. The average characteristic impedance of log-periodic elements is calculated by computing individual impedance as tabulated in Table 2.

Table 2. Impedance calculation of LPE.

Sl. No	Length of the elements $L_{n+1} = \tau L_n$ [mm]	Characteristics Impedance of elements $Z_e = 120 \times \left[\ln\left(\frac{L_e}{D_e}\right) - 2.25\right]\ \Omega$ (14)
1	$L_1 = L_{\max} = 26.3157$	$Z_1 = 266.8980$
2	$L_2 = \tau L_1 = 22.7631$	$Z_2 = 249.4931$
3	$L_3 = \tau^2 L_1 = 19.6901$	$Z_3 = 232.0900$
4	$L_4 = \tau^3 L_1 = 17.0319$	$Z_4 = 214.6880$
5	$L_5 = \tau^4 L_1 = 14.7326$	$Z_5 = 197.2794$
6	$L_6 = \tau^5 L_1 = 12.7437$	$Z_6 = 179.8746$
7	$L_7 = \tau^6 L_1 = 11.0233$	$Z_7 = 162.4748$
8	$L_8 = \tau^7 L_1 = 9.5352$	$Z_8 = 145.0730$
9	$L_9 = \tau^8 L_1 = 8.2479$	$Z_9 = 127.6732$
10	$L_{10} = \tau^9 L_1 = 7.1345$	$Z_{10} = 110.2614$
11	$L_{11} = \tau^{10} L_1 = 6.1713$	$Z_{11} = 92.8600$

The average characteristic impedance is calculated by Eq. (15)

$$Z_a = \frac{\sum_{e=1}^{11} Z_e}{11} \tag{14}$$

3. SIMULATION RESULT AND ANALYSIS

The simulation results obtained from High Frequency Structure Simulation (HFSS v19.2) application details the comparison between hemispherical antennas with and without elements. The preliminary results without elements were not satisfactory according to bandwidth requirement determined through Voltage Standing Wave Ratio (VSWR) ≤ 2. Thus, to improve the performance of hemispherical patch antennas, LPEs are introduced on the hemisphere.

It is observed that LPE plays a vital role in reducing the reflection coefficient (S_{11}) below $-10\,\text{dB}$, thereby improving the impedance bandwidth. The major analysis is carried out by varying $\phi 1$ in the range [33°, 39°] and $\phi 2$ [16°, 17°] which offers the same resonating frequencies over the combinations in relation to Ant_1. These combinations are also advantageous in fabricating the structure. The optimized dimensions of the LPE is as shown in Table 3. The coupling between the elements affects the overall characteristics of the antenna performance. As the spacing between adjacent elements increases, the coupling decreases at higher order frequencies. The non-collinear placement of 4 elements also contributes to reduced coupling between the elements.

The reflection coefficients across different frequency sweep are simulated with and without elements and compared with respect to VSWR and shown in Fig. 5. The input impedance variation with respect to frequency is as shown in Fig. 6.

The magnitude of the impedance is approximately equal to source impedance at resonating frequencies. The antenna offers capacitive impedance of $(47 - j5)\,\Omega$ at 5.1 GHz and inductive impedance

Table 3. Optimized parameters of antenna.

n	1	2	3	4	5	6	7	8	9	10	10 + 1
L_n^* [mm]	26.31	22.76	19.69	17.03	14.73	12.74	11.02	9.53	8.24	7.13	6.17
d_n^{**} [mm]	-	2.46	2.22	2.22	2.22	2.46	4.25	3.79	3.79	3.79	3.79
C_n [mm]	-	2.50	2.25	2.25	2.25	2.50	4.49	3.96	3.96	3.96	3.96

* Measured from surface of the hemisphere.

** Straight line distance d_n (A chord passing through the hemisphere connecting two points) between minor element and major element.

of $(46 + j8)\,\Omega$, $(52 + j3)\,\Omega$, and $(45 + j2)\,\Omega$ at 7.9 GHz, 9.3 GHz, and 13.1 GHz, respectively. The current distributions plotted on the surface of Ant_2 at different resonating frequencies are as given in Fig. 7. The elements have maximal current density at resonating frequency with their length approximately equal to Eq. (5). These elements are active contributors to radiation. The 5th, 10th, and 11th elements actively radiate at 5.1 GHz, 7.9 GHz, and 13.1 GHz, respectively.

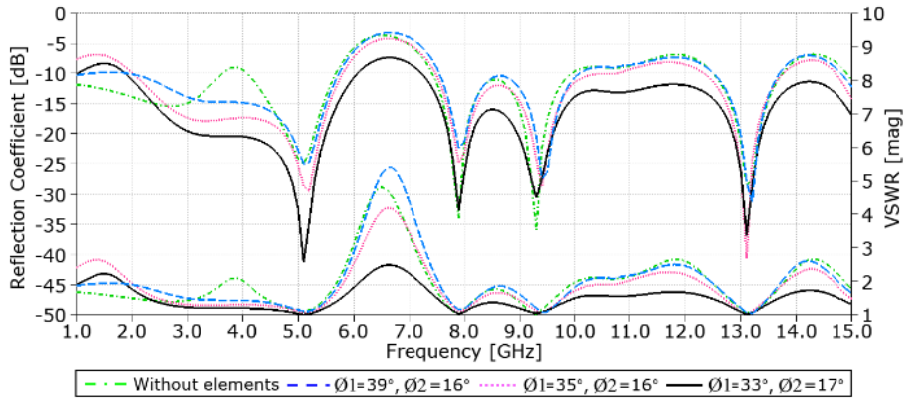

Figure 5. The reflection coefficient (S_{11}) measured in dB (shown in top curve) and the VSWR (shown in the bottom curve) versus frequency plot.

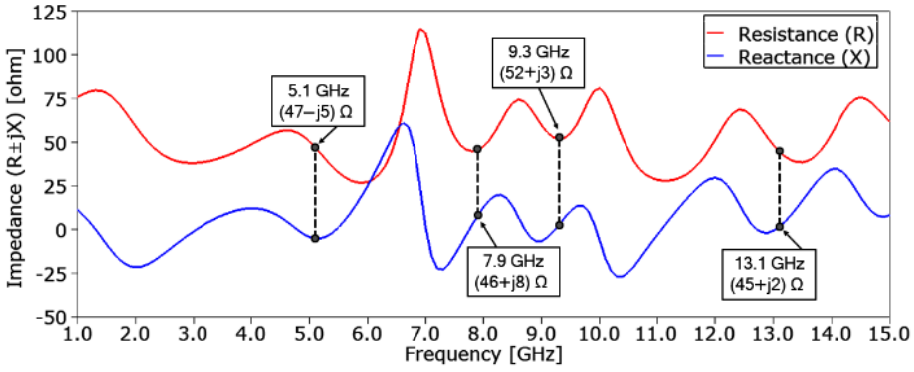

Figure 6. Simulated input impedance variation plotted against frequency for Ant_2 having AoI (33°, 17°).

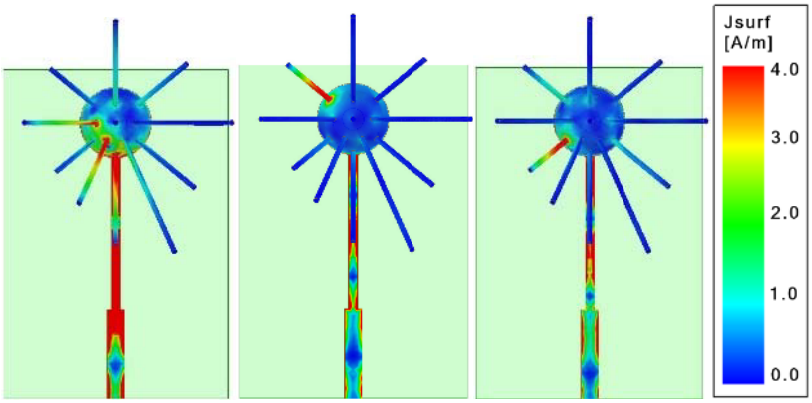

Figure 7. Simulated surface current density (Jsurf) plotted over the Ant_2 having AoI $(33°, 17°)$ at (a) 5.1 GHz, (b) 7.9 GHz and (c) 13.1 GHz.

4. VALIDATION CHARACTERIZATION

In an effort to authorize the simulation conclusions, the submitted antenna is fabricated as given in Fig. 8(a). The RC measurement is recorded using Agilent N5230A PNA series network analyzer, and radiation pattern measurements are recorded by placing the antenna in an anechoic chamber as shown in Fig. 8(b) and Fig. 8(c), respectively. The fabricated antenna is fed through a Reverse Polarity SMA (RP-SMA) connector. The measured results are recorded in the frequency sweep of 1 GHz to 15 GHz. S_{11} lies below -20 dB at resonating frequencies with VSWR < 1.5.

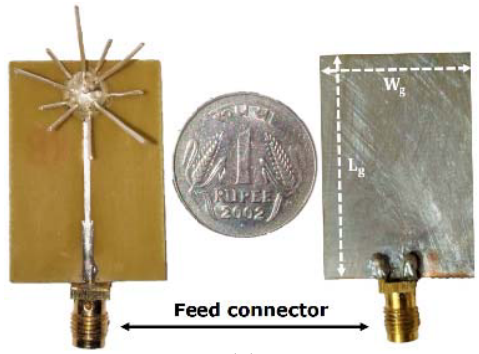

Figure 8. (a) Fabricated structure of the proposed antenna depicting top and bottom planes. (b) Antenna connected to VNA for reflection coefficient measurement. (c) Antenna placed in anechoic chamber for radiation pattern measurement.

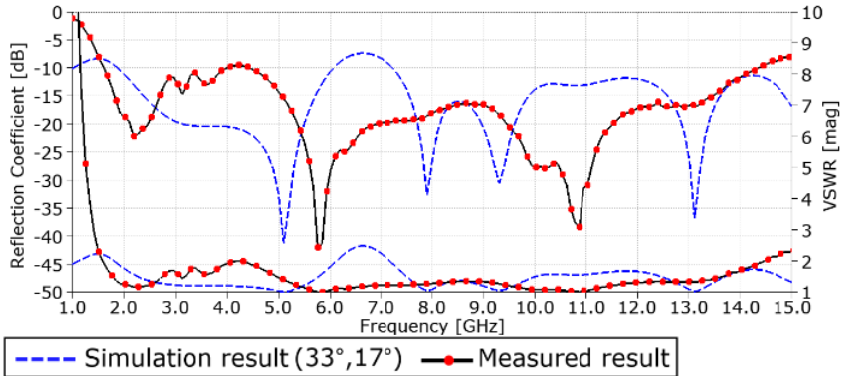

Figure 9. Comparison curves between simulation and measured results. The reflection coefficient (S_{11}) measured in dB (shown in top curve) and the VSWR (shown in the bottom curve) versus frequency plot.

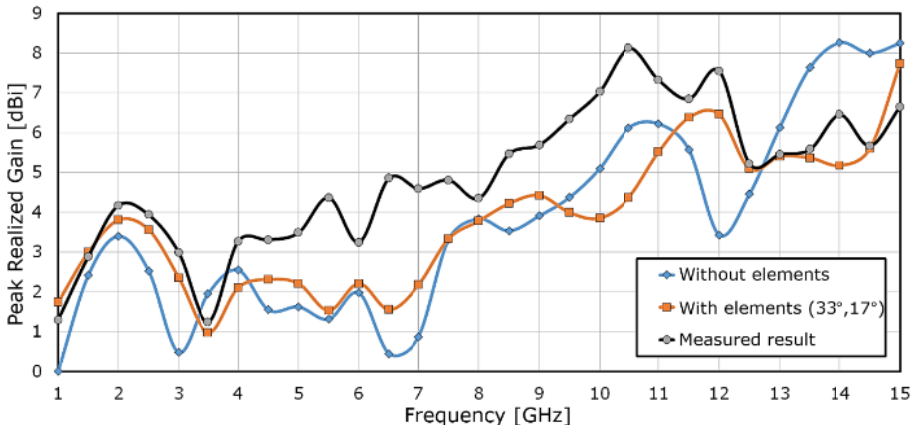

Figure 10. Realized gain comparison between simulation (Ant 1, Ant 2) and measured results.

The antenna satisfactorily operates in the desired frequency range as it is evident in simulation results. The measured S_{11} and VSWR results are compared with the simulation result of Ant_2 as shown in Fig. 9. Higher order frequencies are also present due to surface current distribution over the shorter elements.

Peak Realized Gain (PRG) is the maximum gain over all the directions in far field. The variation of realized gain plotted against frequency is depicted in Fig. 10. There is no significant improvement in the simulated gain performance between the antennas with and without elements. The degradation of gain at some frequencies is due to a multi-directive radiation pattern. The peak gains of the measured antenna were 4.17, 3.24, 4.80, 5.689, 8.12, and 5.45 dBi at frequencies 2.25, 5.79, 7.9, 9.3, 10.5, and 13.1 GHz, respectively.

The impedance matching is acceptable, and the pattern characteristics will not be significantly altered. Some differences between the computer-generated and experimental field patterns are due to the alignment errors, interference, noise, and oxidation of silver. The presented model is the first of its kind, and similar studies are not found till today.

The E-plane (xz and yz-plane) and H-plane (xy-plane) radiation patterns of envisioned antenna are multi-directional, and the polar plot of the simulation and the experimental normalized radiation patterns appear fairly omnidirectional as shown in Figs. 11(a) and (b), respectively. The measured values for radiation pattern are in good agreement with the simulated result and almost omnidirectional in both co-polarized and cross-polarized E and H planes. The multi-directional capability of the hemispherical array will lead to reception of different frequency signals irrespective of the arrival angle. As a result, the antenna is a better receiver.

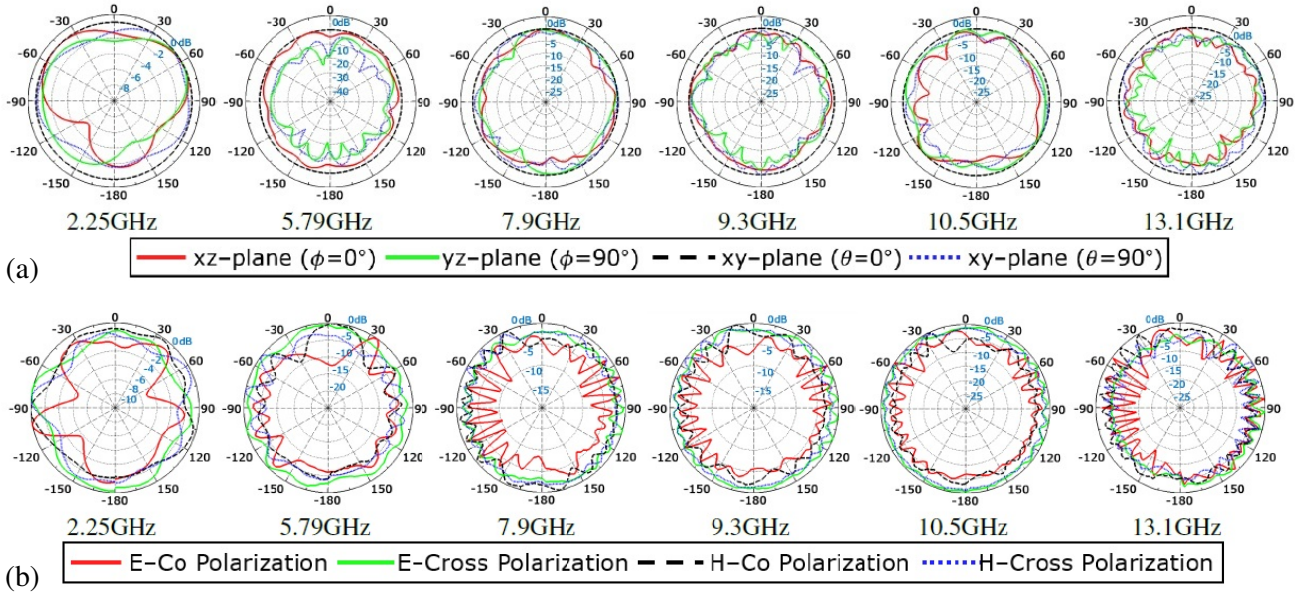

Figure 11. (a) Simulated radiation patterns of Ant 2 normalized to pattern maxima in dB. (b) Measured radiation patterns normalized to pattern maxima in dB.

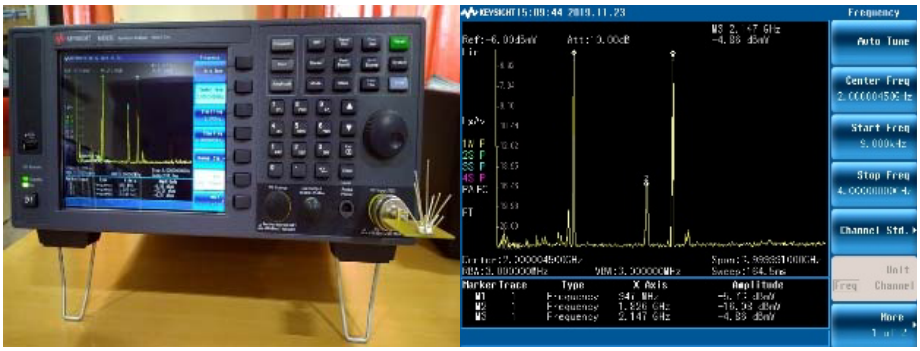

(a) (b)

Figure 12. (a) Antenna connected to spectrum analyzer. (b) Display of frequency channels detected by the antenna in voltage vs time graph.

The trans-receiving capability of the proposed antenna is measured using Keysight N9322C spectrum analyzer as shown in Fig. 12(a). With the 10 dB attenuation and −6 dBmV reference voltage, the antenna measurement is recorded in the frequency range 9 kHz–4 GHz. The antenna is capable of detecting 947 MHz, 1.826 GHz, and 2.147 GHz channels allocated in GSM900 and GSM1800 (Global System for Mobile communication) frequency bands as shown in Fig. 12(b) with the peak amplitude −5.73 dBmV, −16.08 dBmV, and −4.86 dBmV, respectively.

The affinity of the proposed antenna with the prevailing system is assessed by connecting to GSM sim900A module to receive and transmit text messages with mobile terminal over wireless radio frequency (RF) link, worldwide [22]. Considering a 3-phase AC motor setup in irrigational land, the ON/OFF operation of the motor is operated using single pole dual throw (SPDT) relay switch as given in Fig. 13(a) and controlled with atmega2560 micro-controller. The relay can be turned on/off by definite text commands to enable or disable the state of the AC motor as sent by the user. The physical model of the GSM based AC motor is controlled using a micro-controller with the envisioned antenna positioned in irrigational land as given in Fig. 13(b). The proposed antenna can receive transmitted text commands to verify the motor state to the user via SMS (Short Message Service). The motor will

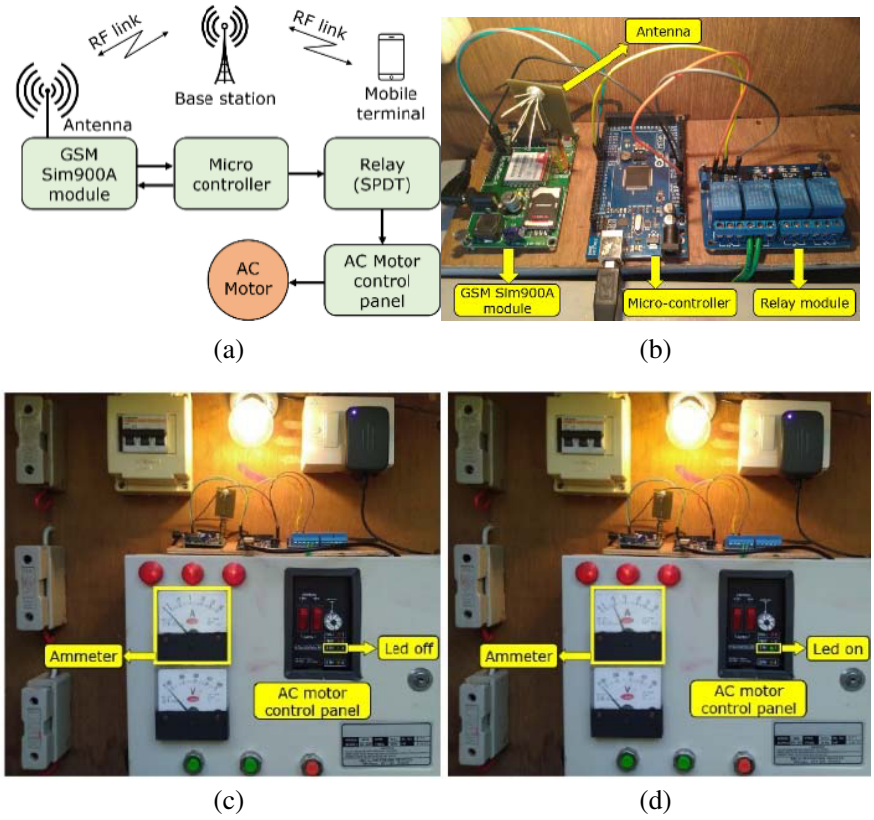

Figure 13. (a) Functional overview. (b) Experimental setup. (c) Motor in OFF state with ammeter reading 0 A. (d) Motor in ON state with ammeter reading 9 A.

be deenergized upon receiving OFF command resulting in no deflection in the ammeter as shown in Fig. 13(c). The motor will be energized by ON command resulting in deflection in ammeter as given in Fig. 13(d).

5. CONCLUSION

This paper puts forth a novel approach which highlights the effect of Log-Periodic Elements (LPEs) in achieving higher bandwidth, reduced S_{11} below -20 dB, and multi-directive radiation pattern. Prototype of the antenna was simulated, tested, verified, and compared with simulation results. The proposed antenna has a -10 dB impedance bandwidth of 158% from 1.68 GHz to 14.31 GHz (8.52 : 1) in measurement and suitable for UWB applications.

The measured results has fewer resonating peaks than simulation results due to mechanical discontinuities while the antenna structure is fabricated. The formation of silver dioxide on hemisphere and microairgaps in the hemisphere caused the difference between measurement and simulation results.

Due to variation in placing the elements on the surface of hemisphere, a few inconsistencies are found between simulated and measured results.

REFERENCES

1. Hoffman, M., "Conventions for the analysis of spherical arrays," *IEEE Transactions on Antennas and Propagation*, Vol. 11, No. 4, 390–393, Jul. 1963.
2. Tang, M., X. Chen, M. Li, and R. W. Ziolkowski, "Particle swarm optimized, 3-D-printed, wideband, compact hemispherical antenna," *IEEE Antennas and Wireless Propagation Letters*, Vol. 17, No. 11, 2031–2035, Nov. 2018.

3. Chen, J., J. Ludwig, and S. Lim, "Design of a compact log-periodic dipole array using T-shaped top loadings," *IEEE Antennas and Wireless Propagation Letters*, Vol. 16, 1585–1588, 2017.
4. Bozdag, G. and A. Kustepeli, "Subsectional tapered fed printed LPDA antenna with a feeding point patch," *IEEE Antennas and Wireless Propagation Letters*, Vol. 15, 437–440, 2016.
5. Zhou, Y., J. Huang, W. Wu, and N. Yuan, "Conformal LPDA antenna array for direction finding application," *2016 IEEE International Conference on Microwave and Millimeter Wave Technology (ICMMT)*, 2016.
6. Deng, C., Y. Li, Z. Zhang, and Z. Feng, "A hemispherical 3-D null steering antenna for circular polarization," *IEEE Antennas and Wireless Propagation Letters*, Vol. 14, 803–806, 2015.
7. Hui, H. T., K. N. Yung, C. L. Law, Y. S. Koh, and W. L. Koh, "Design of small and low profile 2/spl times/2 hemispherical helical antenna array for mobile satellite communication," *IEEE Transactions on Antennas and Propagation*, Vol. 52, No. 1, 346–348, Jan. 2004.
8. Goossens, R., I. Bogaert, and H. Rogier, "Phase-mode processing for spherical antenna arrays with a finite number of antenna elements and including mutual coupling," *IEEE Transactions on Antennas and Propagation*, Vol. 57, No. 12, 3783–3790, Dec. 2009.
9. Braaten, B. D., S. Roy, I. Irfanullah, S. Nariyal, and D. E. Anagnostou, "Phase-compensated conformal antennas for changing spherical surfaces," *IEEE Transactions on Antennas and Propagation*, Vol. 62, No. 4, 1880–1887, Apr. 2014.
10. Franek, O., G. F. Pedersen, and J. B. Andersen, "Numerical modeling of a spherical array of monopoles using FDTD method," *IEEE Transactions on Antennas and Propagation*, Vol. 54, No. 7, 1952–1963, Jul. 2006.
11. Baee, R. K., K. Forooraghi, and S. Chamaani, "Conformal array pattern synthesis using a hybrid WARP/2LB-MOPSO algorithm," *International Journal of Antennas and Propagation*, Vol. 2012, 2012.
12. Meiguni, J. and D. Pommerenke, "Theory and experiment of UWB archimedean conformal spiral antennas," *IEEE Transactions on Antennas and Propagation*, Vol. 67, No. 10, 6371–6377, Oct. 2019.
13. Zhang, B., J. Kovitz, and Y. Rahmat-Samii, "A hemispherical monopole rectenna array for multi-directional, multi-polarization and multi-band ambient RF energy harvesting," *IEEE International Symposium on Antennas and Propagation (APSURSI)*, 603–604, Fajardo, 2016.
14. Famoriji, O. J., K. Akingbade, E. Ogunti, W. Apena, A. Fadamiro, and F. Lin, "Analysis of phased array antenna system via spherical harmonics decomposition," *IET Communication*, Vol. 13, No. 18, 5434–5454, Dec. 2019.
15. Howell, J. Q, "Microstrip antennas," *IEEE Transactions on Antennas and Propagation*, Vol. 23, 90–93, Jan. 1975.
16. Garg, R., P. Bhartia, I. Bahl, and A. Ittipiboon, *Microstrip Antenna Design Handbook*, Artrech House, Norwood, Mass, 2001.
17. Isbell, D. E., "Log periodic dipole arrays," *IRE Transaction on Antennas and Propagation*, Vol. 8, 260–267, May 1960.
18. Patel, M., V. S. Jadaun, K. Lal, and P. Kuchhal, "Design of a high gain compact circular microstrip patch antenna for X-band," *International Journal of Engineering and Technology*, Vol. 7, No. 2.6, 168–170, 2018.
19. Lo, Y. T. and S. W. Lee, *Antenna Handbook: Theory, Applications, and Design*, Springer Science & Business Media, 2013.
20. Monticone, L. C., R. E. Snow, and F. Box, "Minimizing great-circle distance ratios of undesired and desired signal paths on a spherical earth," *IEEE Transactions on Vehicular Technology*, Vol. 58, No. 9, 4868–4877, Nov. 2009.
21. DuHamel, R. H. and D. E. Isbell, "Broadband logarithmically periodic antenna structures," *IRE National Convention Record*, Pt. 1, 119–128, 1957.
22. Dhanush Gowda, E. and V. Nuthan Prasad, "Design of log-periodic monopole array patch antenna for UWB applications using alphabetic slots on partial ground plane," *2020 IEEE International Conference on Electronics, Computing and Communication Technologies (CONECCT)*, 1–5, 2020.